PAPER

Check for updates

Plasmonic Ag decorated CdMoO₄ as an efficient photocatalyst for solar hydrogen production†

Yogesh A. Sethi,[a] Aniruddha K. Kulkarni,[b] Supriya K. Khore,[a] Rajendra P. Panmand, [ID][c] Sandip C. Kanade,[d] Suresh W. Gosavi,[e] Milind V. Kulkarni*[a] and Bharat B. Kale [ID] *[a]

The synthesis of Ag-nanoparticle-decorated CdMoO₄ and its photocatalytic activity towards hydrogen generation under sunlight has been demonstrated. The CdMoO₄ samples were synthesized by a simple hydrothermal approach in which Ag nanoparticles were *in situ* decorated on the surface of CdMoO₄. A morphological study showed that 5 nm spherical Ag nanoparticles were homogeneously distributed on the surface of CdMoO₄ particles. The UV/DRS spectra show that the band gap of CdMoO₄ was narrowed by the incorporation of a small amount of Ag nanoparticles. The surface plasmonic effect of Ag shows broad absorption in the visible region. The enhanced photocatalytic hydrogen production activities of all the samples were evaluated by using methanol as a sacrificial reagent in water under natural sunlight conditions. The results suggest that the rate of photocatalytic hydrogen production using CdMoO₄ can be significantly improved by loading 2% Ag nanoparticles: *i.e.* 2465 μmol h^{-1} g^{-1} for a 15 mg catalyst. The strong excitation of surface plasmon resonance (SPR) absorption by the Ag nanoparticles was found in the Ag-loaded samples. In this system, the role of Ag nanoparticles on the surface of CdMoO₄ has been discussed. In particular, the SPR effect is responsible for higher hydrogen evolution under natural sunlight because of broad absorption in the visible region. The current study could provide new insights for designing metal/semiconductor interface systems to harvest solar light for solar fuel generation.

1. Introduction

Rapid energy consumption and decreasing natural resources of fossil fuels and extensive global energy demands have stimulated the development of sustainable energy production systems from renewable sources.[1,2] It is high time that eco-friendly and cost-effective, alternative energy is made a key target for the development of renewable energy sources. Among various renewable resources, solar light assisted hydrogen (H₂) generation using semiconductors is an attractive step in the direction of sustainable energy production.[3–5] Sunlight is the most abundant, highly energy efficient, nonpolluting, inexpensive source for harvesting and conversion into storable

chemical energy by mirroring the natural photosynthesis process. It can address our future energy demands since photocatalytic H₂ generation under sunlight is considered to be a "fuel for the future".[6] The sunlight assisted water-splitting reaction in the hydrogen evolution reaction (HER) (HER: $2H^+ + 2e^- \rightarrow H_2$), requires a large free energy change to trigger the reaction.[7]

This can be made possible only by using the narrow band gap of a semiconductor which can absorb light under sunlight.[8] However, ideal semiconductor photocatalysts for hydrogen generation from water are limited, due to several requirements such as good absorption capability, suitable band edge position, efficient charge separation and transport, chemical stability in an aqueous environment, which are basic challenges in achieving solar energy conversion efficiency.[9,10] To overcome these issues, developing a highly active semiconductor photocatalyst is still a great challenge worldwide. In the past, various semiconductors have been reported for photocatalytic hydrogen generation, such as ZnO,[11] TiO₂,[12] Ta₂O₅,[13] CdS,[14] ZnS,[15] Nb₂O₅,[16] and WO₃.[17]. These binary metal oxides show great potential for solar energy conversion efficiency. However, their activity for hydrogen generation is not economical due to their unsuitable indirect band edge position, low charge transport, high resistivity, poor stability *etc.*[18,19] Earlier reports show that anion doping in potential catalysts such as TiO₂,[20] or ZnO,[21]

[a]Nanocrystalline Laboratory, Centre for Material for Electronic Technology (CMET), Ministry of Electronics and Information Technology, Govt. of India, Panchawati, Off Pashan Road, Pune 411007, India. E-mail: bbkale1@gmail.com; bbkale@cmet.gov.in; Fax: +91 20 2589 8180; Tel: +91 20 2589 9273

[b]Prof. John Barnabas School for Biological Study, Ahmednagar College, Ahmednagar, India, 414001

[c]Centre for Material for Electronic Technology (CMET), Ministry of Electronics and Information Technology, Govt. of India, Trissure, Kerala 680581, India

[d]Department of Chemistry, IISER, Pune 411008, India

[e]Department of Physics Savitribai Phule University, Pune, India, 411008

† Electronic supplementary information (ESI) available. See DOI: 10.1039/c9ra05581a

tunes the band gap in the visible region and significantly improves photocatalytic activity, but doping sites act as recombination centers, leading to poor activity and poor sustainability due to photo-corrosion. To overcome the problems of binary metal oxides, it is crucial to develop a multi-component photocatalyst which shows good photocatalytic activity in the visible region with excellent stability. In the past, molybdenum-based semiconductors gained a lot of attention because of their wide range of technological applications, such as hydrogen generation,[22] organic pollutant degradation,[23] Li-ion batteries,[24] and solar cells.[25] Among all molybdenum-based semiconductors, $CdMoO_4$ is an interesting semi-conductor due to its unique scheelite-type structure, exotic electronic structure, and better optical properties.[26] Historically, there have been only a few reports available on the photocatalysis by $CdMoO_4$ such as $CdS/CdMoO_4$ (ref. 27 and 28a) being used for dye degradation. Our group has reported $CdMoO_4$–graphene for the water splitting reaction.[28b] However, photocatalysis applications have been less explored due to its wide band gap (3.2 eV). Previous reports show that the integration of plasmon active metals (Ag, Au, Cu) on the surface of passive oxide semiconductors also helps to enhance charge transfer kinetics.[29a]

The enhancement of the photocatalytic activity of a semi-conductor due to noble metals may take place in the following ways. (1) The noble metal NPs absorb visible light, in which photogenerated electrons and holes are separated by the metal–semiconductor interface, and the oxidation and/or reduction reactions take place on the surface of the noble metal–semi-conductor. This mechanism involves the transfer of photo-generated electrons and/or holes from the noble metal NPs to the semiconductors. (2) Radiative energy transfer can take place from the noble metal NPs to the semiconductor through the interaction of the semiconductor with the strong SPR-induced electric field localized in the immediate vicinity of the noble metal NPs. This SPR-induced electric field can enhance the rate of electron–hole formation, especially on the surface of the semiconductor. Then the photogenerated electrons and holes are easily transferred to the semiconductor/liquid interface, enhancing the photocatalytic efficiency.[29b,29c] The surface plasmon resonance (SPR) transfers electrons from the metal to the semiconductor and tunes the optical properties of the semi-conductor photocatalyst.[30] Therefore, one approach to overcoming a wide band gap semiconductor is to decorate noble metal nanoparticles onto its surface. According to Adhikari et al.,[31] the presence of Ag nanoparticles on $CdMoO_4$ enhances the charge carrier separation efficiency and photocatalytic activity for dye degradation. An optimum and designed nano-composite would result in strong electronic interaction between $CdMoO_4$ and Ag nanoparticles that would show enhanced photocatalytic activity in visible light.

In this context, we have successfully synthesized an $Ag@CdMoO_4$ heterostructured photocatalyst through a facile hydrothermal method by decorating Ag nanoparticles onto the surface of $CdMoO_4$. The as-prepared heterostructure photo-catalyst was examined for hydrogen generation under natural sunlight. The resultant $Ag@CdMoO_4$ heterostructured photocatalyst exhibits significantly enhanced photocatalytic activity for hydrogen evolution under solar light irradiation.

2. Experimental sections

Sodium molybdate di-hydrate $(Na_2MoO_4) \cdot 2H_2O$, cadmium nitrate $(Cd(NO)_2 \cdot 4H_2O)$ and $Ag(NO)_3$ silver nitrate used for the preparation of the catalysts are of analytical grade (SD Fine-Chem Limited, India) and used without any further purification.

2.1 Synthesis of Ag@CdMoO₄

All the chemicals used for the synthesis of $Ag–CdMoO_4$ were analytical grade and used without further purification. $Ag–CdMoO_4$ photocatalysts were synthesized by a hydrothermal method and the procedure is briefly described as follows: firstly, 0.05 mole of cadmium nitrate tetrahydrate $(Cd(NO_3)_2 \cdot 4H_2O)$ (99.99%) and 0.05 mole of sodium molybdate Na_2MoO_4 (99.99%) were mixed in 50 mL of water in a separate beaker (a). Similarly, 0.5 wt% silver nitrate solution was prepared in 10 mL double distilled water in another beaker (b) and added to the above mixture (a). The clear solution was then transferred to a 200 mL capacity Teflon autoclave and kept at 180 °C for 24 h in an electric oven. The synthesized catalyst was washed several times with absolute ethanol and deionized water, and a brown-colored powder was obtained. This sample was marked CMAg-0 and used for further analysis and comparison. Similarly, different concentrations of silver nitrate solution, 0, 0.5, 1, 2, and 3 wt%, were prepared and a procedure similar to that mentioned above was followed in order to synthesize the other samples. Hence, five samples were prepared for comparative purposes and each sample obtained was labelled CMAg-0, CMAg-0.5, CMAg-1, CMAg-2, CMAg-3, respectively, for convenience.

2.2 Photocatalytic study

2.2.1 Photocatalytic hydrogen generation from water. The photochemical reaction was carried in a 70 mL total volume air-tight cylindrical quartz reactor with a cooling jacket for water circulation. All the reactions were carried out under ambient conditions under natural sunlight on sunny days (March to May) between 10 am and 3 pm at Pune, located in the Maharashtra state of India. The intensity of solar light was measured using a digital lux meter. The measured average intensity of solar light reaching the surface of the earth was 145 000 lux. In a typical photocatalytic experiment, 15 mg of the photocatalyst was dispersed in 25 mL total volume containing 20% methanol (v/v) in aqueous solution. The 45 mL free space of the photo-reactor was made airtight with a rubber septum followed by ultrasonication for 5 min for the uniform dispersion of catalyst. The solution mixture was then purged with Ultra High Purity nitrogen gas (UHP 99.999%) to remove all the gases in the headspace of the reactor and dissolved oxygen from the reaction mixture. Before and after irradiation with solar light, the gas in the free space of the reactor was analyzed using gas

chromatography (GC). The generated gas was analyzed immediately using GC over a specific time interval.

2.3 Sample characterization

The phase formation and crystallite size of all synthesized samples were estimated *via* X-ray diffractometry (XRD-D8, Advance, Bruker-AXS) with Ni-filtered Cu-Kα radiation ($\lambda = 1.5418$ Å). Optical properties of the bare and Au loaded samples were studied by a UV-Vis-DRS spectrophotometer (UV 2600 spectrometer, Lambda-950, PerkinElmer) in the spectral range 200–800 nm. The surface morphology was characterized using field emission scanning electron microscopy (FESEM; Hitachi, S-4800 II) and field emission transmission electron microscopy (FETEM; JEM-2000 FS). Image processing and interplanar distance (d) evaluation were performed with the help of micrograph Gatan software. Raman scattering (RS) was performed at room temperature using an HR 800-Raman spectrometer (Horiba Jobin Yvon, France) with excitation at 532 nm by a coherent He–Ne ion laser and a liquid nitrogen cooled CCD detector to collect and process the backscattered data. Surface characterization of all Ag@CdMoO$_4$ samples was carried out using X-ray photoelectron spectroscopy (XPS, ESCA-3000, VG Scientific Ltd.) at a pressure of $>1 \times 10^{-9}$ Torr. The general scan C 1s, O 1s, Ag 1s, and Cd 2p core level spectra were recorded with non-mono-chromatized Mg-Kα radiation (photon energy 1253.6 eV). Baseline correction and peak fitting for all the samples were done using the software package XPS Peak. The core level binding energies (BEs) were aligned with respect to the C 1s binding energy of 285 eV. The collected gas sample was analyzed using a gas chromatography system (GC, Shimadzu GC- 2014) with a Porapak-Q packed column coupled with a TCD detector and using nitrogen (N2-UHP) as a carrier gas.

3. Results and discussion

3.1 Structural study

The CdMoO$_4$ and Ag loaded CdMoO$_4$ samples were synthesized by a hydrothermal method at 180 °C for 24 h. The phase purity of pristine CdMoO$_4$ and Ag decorated CdMoO$_4$ were investigated by their powder X-ray diffraction pattern. Fig. 1 shows the powder XRD patterns of bare CdMoO$_4$ and Ag decorated CdMoO$_4$ samples. Fig. 1(a) shows the XRD pattern of bare CdMoO$_4$ (CMAg-0) which matches well with (JCPDS no. 00-007-0209) of tetragonal phase CdMoO$_4$ having a scheelite-type structure.[32] Fig. 1(b–e) show XRD patterns of Ag decorated CdMoO$_4$, compared with pure CdMoO$_4$. Additional reflection peaks at $2\theta = 38.37°$, $44.78°$, and $64.81°$ are observed, which indicate the presence of Ag and are indexed as the (1 1 1), (2 0 0) and (2 2 0) crystallographic planes of Ag NPs, respectively. These peaks match well with face centered cubic (FCC) metallic Ag NPs (JCPDS card no. 04-0783). For a lower Ag concentration (0.5%) the separate peaks are not clearly observed as it is below the detection limit. Further, it is observed that, with an increase in the concentration of Ag on CdMoO$_4$ the intensity of the Ag
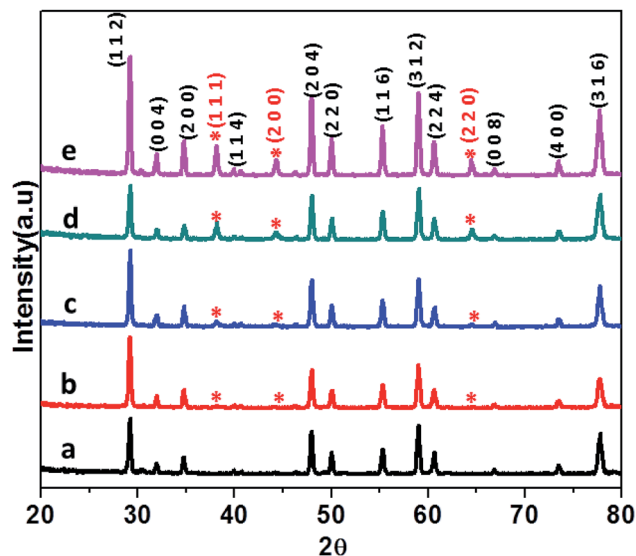

Fig. 1 XRD patterns of (a) pure CdMOO$_4$, (b) 0.5% Ag@CdMoO$_4$, (c) 1% Ag@CdMoO$_4$, (d) 2% Ag@CdMoO$_4$, (e) 3% Ag@CdMoO$_4$ sample photocatalyst.

peaks increases. It is also observed that there are no large shifts in the positions of the diffraction peaks, which further confirms that the as-synthesized samples are composed of CdMoO$_4$ and Ag phases.

3.2 Surface and morphological studies

Fig. 2(a–j) show FE-SEM images of the as-prepared CdMoO$_4$ as well as Ag–CdMoO$_4$. The morphology can be seen in a different magnification. From the panoramic view (Fig. 2), it can be seen that the samples are composed of a uniform polyhedron with a relatively regular size distribution and a large aspect ratio. The magnified FE-SEM image (Fig. 2(b)) of the sample (CMAg-0) shows polyhedron-shaped particles of CdMoO$_4$ with sizes in the range 900–1000 nm. Furthermore, Fig. 2(c and d) show the same particle morphology with sizes in the range 800–1000 nm along with the rear density of Ag nanoparticles of 50–100 nm (sample CMAg-0.5). With an increase in the Ag content, agglomeration and coalescence have occurred. Also, the Ag particle density has increased. For sample CMAg-1, the same particle morphology was observed in Fig. 2(e and f), having sizes of 900–1000 nm for CdMoO$_4$ along with dense Ag nanoparticles of sizes 50–100 nm. These particles are uniformly distributed with a smooth and flat surface. The increase in Ag content will increase the rate of diffusion with the coalescence process of neighboring grains which effects an increase in particle size and crystal growth. Moreover, XPS and EDS mapping analysis were performed to support the chemical composition and elemental analysis of the CdMoO$_4$ samples and the results show the presence of Ag, Cd, Mo and O elements.

Further, FETEM investigations were performed in order to determine the morphology and crystalline nature of the pristine CdMoO$_4$ microsphere sample and the results are shown in Fig. 3(a–d). The microspheres can be seen in the TEM image in
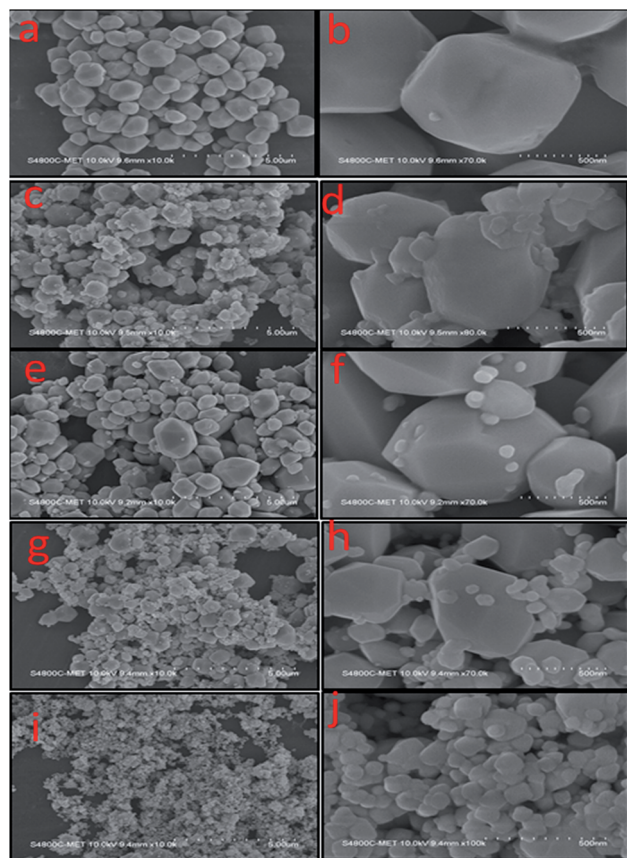
Fig. 2 FESEM images of (a and b) pure $CdMoO_4$, (c and d) 0.5% Ag@$CdMoO_4$, (e and f) 1% Ag@$CdMoO_4$, (g and h) 2%, (i and j) 3% Ag@$CdMoO_4$ sample photocatalyst.

Fig. 3(a). The corresponding TEM images of the $CdMoO_4$ microspheres show an ordered uniform structure. A nanoprism is observed at the edge of a $CdMoO_4$ microsphere, which clearly reveals that the microspheres are composed of nanoprisms (Fig. 3b and c). The measured size of the prism is 800–1000 nm (Fig. 3a and b), which is also in good agreement with the results from the FE-SEM analysis. Fig. 3(c) clearly resolves the lattice fringes of the CMAg-0 sample. The interplanar spacing, *i.e.* 0.305 nm, can be indexed to the (1 1 2) plane of tetragonal $CdMoO_4$. Fig. 3(d) shows the selected area electron diffraction (SAED) pattern of the $CdMoO_4$ sample, which clearly shows the crystalline nature of the sample. Fig. 4(a–d) show the FETEM images of Ag decorated $CdMoO_4$ microspheres. Fig. 4(a–b) show the polyhedron of $CdMoO_4$ of size 500–900 nm along with the Ag nanoparticles of size 30–40 nm decorated on its surface. Fig. 4(c–d) show the high-resolution transmission electron microscope (HRTEM) images taken from the edge of a nanoparticle, which provide more detailed structural information. Fig. 4(c and d) reveal the lattice fringes of the heterostructure. The interplanar spacing, *i.e.* 0.305 nm, can be indexed to the (1 1 2) plane of tetragonal $CdMoO_4$, while 0.250 nm corresponds to that of the (1 1 1) lattice plane of cubic Ag. The corresponding SAED pattern of the heterostructure represents the crystalline nature of the material (Fig. 4d). Furthermore, Fig. 5(a–d) show
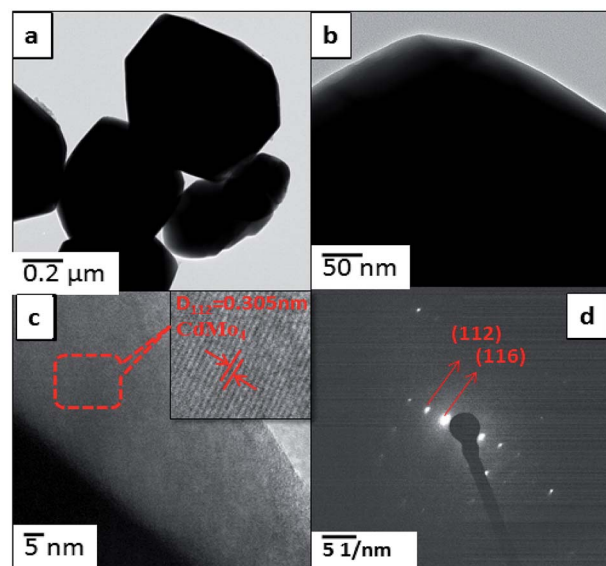

Fig. 3 FE-TEM images of pure $CdMoO_4$: (a and b) TEM images, (c) HR-TEM image and (d) SAED pattern.

TEM mapping results of Ag@$CdMoO_4$ and clearly show the presence of Cd, Mo, O, and Ag. Fig. 6 clearly shows the presence of Ag on the surface of the $CdMoO_4$ polyhedron.

3.3 Optical and electronic studies

The optical properties of $CdMoO_4$ and Ag@$CdMoO_4$ were studied by UV-Vis spectroscopy (Fig. 6). As shown in Fig. 6, a significant absorption edge at wavelength 380 nm was observed, which is assigned to the band gap absorption edge of $CdMoO_4$ and the band gap is calculated to be 3.2 eV, which is slightly lower than the previously reported band gap.[33] The slight deviation in band gap is due to the larger particle size.
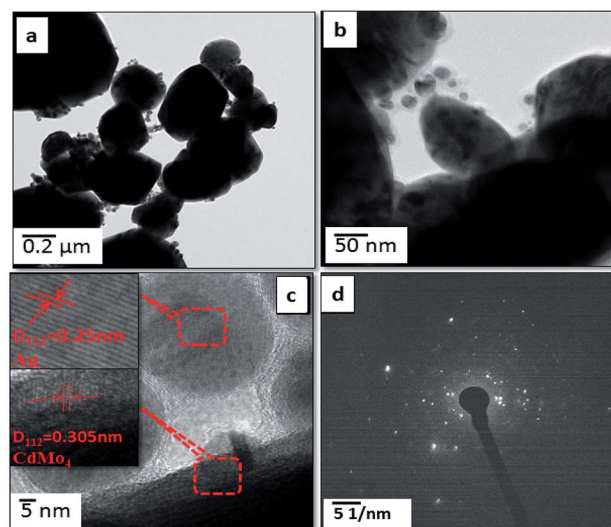

Fig. 4 FE-TEM images of 2% Ag@$CdMoO_4$: (a and b) TEM images, (c) HR-TEM image and (d) SAED pattern.
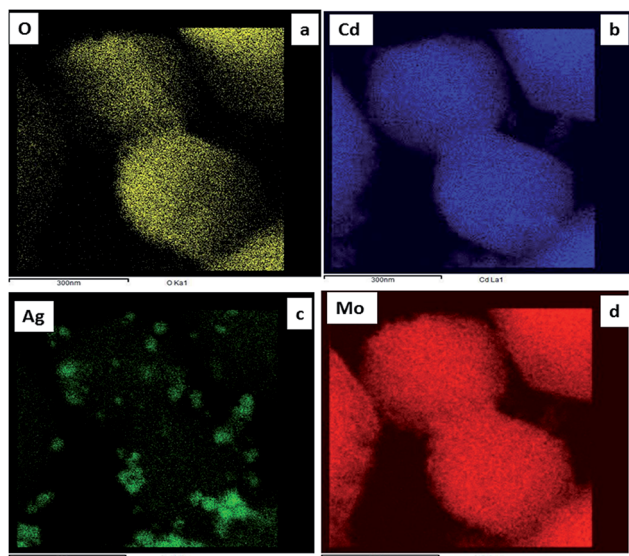
Fig. 5 FE-TEM mapping images of (a–d) 2% Ag@CdMoO$_4$ (CMAg-2).

Fig. 6 (CMAg-1 to CMAg-3), shows alignment with the absorption edge of the CdMoO$_4$ (~420 nm) band gap of 2.9 eV. Also, Ag NP decorated CdMoO$_4$ samples show a strong broad absorption band at around 480 nm, which is attributed to the surface plasmon resonance (SPR) effect caused by the Ag nanoparticles.[34] The strong appearance of SPR at 480 nm further confirms the presence of Ag on CdMoO$_4$. The higher value of SPR (480 nm) is due to the size and shape of the Ag nanoparticles and the surrounding liquid medium. It is also observed that, with an increase in Ag concentration, the intensity of the SPR peak with respect to the intensity of the absorption edge at 380 nm also increases in the visible region, which may be due to lowering of the CdMoO$_4$ surface for photon absorption as Ag nanoparticles cover a greater surface area of CdMoO$_4$.
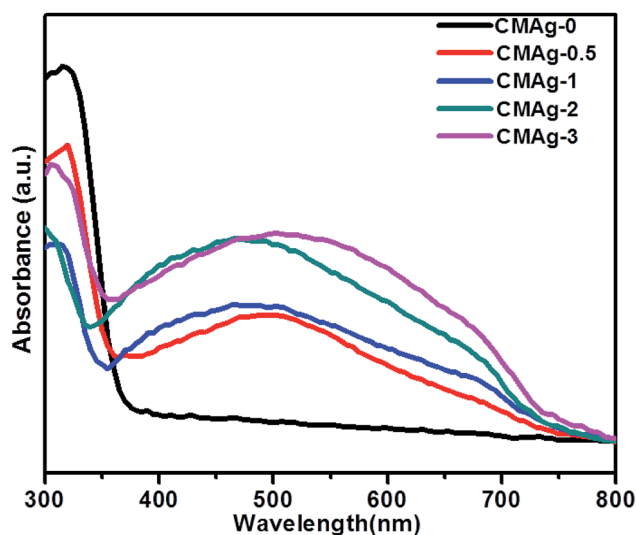

Fig. 6 UV-Vis absorption spectra of CdMoO$_4$ and Ag decorated CdMoO$_4$.

Photoluminescence (PL) is a unique tool to study the migration separation recombination process of photogenerated charge carriers from semiconductor materials. Fig. 7 shows a comparative study of the PL spectra of CdMoO$_4$ and Ag decorated CdMoO$_4$ excited at a wavelength of 325 nm at room temperature. Pure CdMoO$_4$ shows a strong UV emission peak at 340 nm, which is regarded as coming from the charge transfer transition between the O 2p orbital and Mo 3d orbital from the MoO$_4^{2-}$ ions complex from CdMoO$_4$.[36,37] The UV emission peak could be assigned to the near band edge emission of the CdMoO$_4$ band gap. The Ag decorated CdMoO$_4$ shows a strong emission peak at 530–540 nm along with some weak peaks also observable at 450–500 nm.[35] The peak could be assigned to the presence of Ag NPs on the surface of CdMoO$_4$ decreasing surface defects and suppressing charge carrier recombination, which is good for improving the photocatalytic activity. In addition to that, the emission peak intensity of CdMoO$_4$ is lowered with the addition Ag NPs, which is in accordance with Stern–Volmer quenching.[38,39] The lower peak intensity indicates a lower electron–hole pair recombination rate, and an increase in the lifetime of photogenerated charge carriers is expected to enhance photocatalytic activity.[40] In general, photocatalytic activity depends mainly upon the electron–hole pair separation rate, and an optimized amount of Ag NPs shows a large charge utilization for the redox reaction compared with bare CdMoO$_4$.

3.4 Raman study

Raman spectroscopy is an important and powerful tool to characterize the crystallinity of a material and for phase identification. Fig. 8 shows the Raman spectra of pure and Ag decorated CdMoO$_4$ using a 532 nm laser source. Raman spectra with different concentrations of Ag decorated on CdMoO$_4$ and pure CdMoO$_4$ show some additional absorption bands, apart from those recorded for Ag–CdMoO$_4$. In general, for molybdates with a scheelite-type crystal structure the active frequencies in Raman spectra are observed in the range of wavenumbers 900 to 750 cm^{-1} (stretching modes ν1 and ν3) and 450–250 cm^{-1} (bending modes ν2 and ν4).[41] The observed peaks for the stretching modes of Mo–O bonds in MoO$_4$ tetrahedra are at 867, 825 and 761 cm^{-1}, and the absorption bands with their maxima at 399, 310, 309, and 277 cm^{-1} can be related to the bending modes of Mo–O bonds in distorted MoO$_4$ tetrahedra with a cationic vacancy near one or two corners of the MoO$_4$ tetrahedron, which are characteristic of CdMoO$_4$.[42,43] Similar results were observed in 0.5% Ag decorated CdMoO$_4$. But, at a high concentration of Ag (2%) only the characteristics peaks of CdMoO$_4$
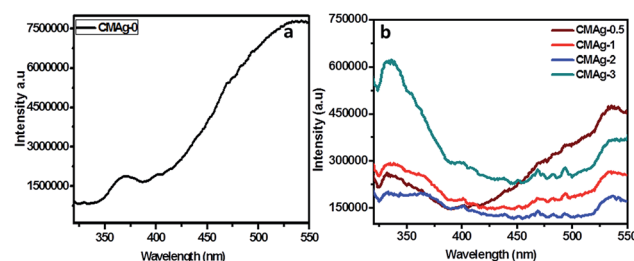

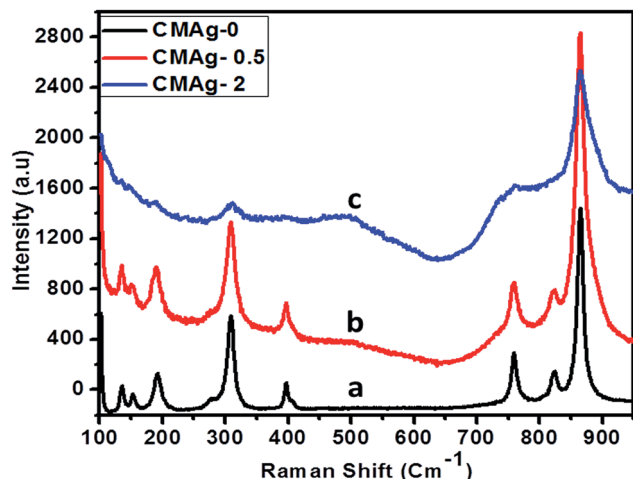**Fig. 7** PL spectra of (a) CdMoO$_4$, (b) Ag decorated CdMoO$_4$.

Fig. 8 Raman spectra of (a) CMAg-0, (b) CMAg-0.5, (c) CMAg-2.

Fig. 9 XPS spectra of the as-prepared $CdMoO_4$ (black line) and $Ag@CdMoO_4$ (red line) sample: (a) survey, (b) Cd, (c) Mo, (d) O (e) Ag.

were observed: *i.e.* 867 cm^{-1} stretching Mo–O bonds and 310 cm^{-1} bending Mo–O bonds in distorted MoO_4 tetrahedra were observed, but minor peaks were not observed because of the high concentration of Ag on the $CdMoO_4$ surface. Similar results were observed in case of Ag–TiO_2.[44]

3.5 XPS study

The chemical composition and binding energy states of pristine $CdMoO_4$ and Ag decorated $CdMoO_4$ were investigated by X-ray photoelectron spectroscopy. Fig. 9(a) shows a comparative survey spectrum of $CdMoO_4$ and Ag decorated $CdMoO_4$, which indicates the existence of Ag, Cd, Mo and O elements. Fig. 9(b) shows the high-resolution spectra of sample CMAg-0 for the Cd 3d state at a binding energy of 403.01 eV, whereas for sample CMAg-2 a Cd 3d peak was located at a binding energy of 402.91 eV.[45] Fig. 9(c) shows the peaks for Mo 3d in sample CMAg-0 located at binding energies of 230.28 and 232.12 eV, attributed to Mo $3d_{5/2}$ and Mo $3d_{3/2}$ states of the Mo(VI) orbital, respectively.[46] Similarly, peaks in the spectrum sample CMAg-2 shifted to 232.0 and 235.2 eV and are ascribed to Mo $3d_{5/2}$ and Mo $3d_{3/2}$ of the Mo(VI) orbital, respectively, being 0.1 eV higher than the corresponding two peaks in the Mo(VI) in the CMAg-0 sample.[47] Fig. 9(d) shows the O 1s spectra for pure $CdMoO_4$ and the Ag decorated $CdMoO_4$ samples CMAg-0 and CMAg-2 both show a strong symmetric peak at a binding energy of 528 eV, which may be due to Cd–O and Mo–O bonds, respectively. Fig. 9(d) shows Ag 3d peaks located at a binding energy of 368.82 eV, and splitting of the 3D doublet at 374 eV is attributed due to presence of reduced silver nanoparticles on the surface of $CdMoO_4$.[48] From the above results it is clear that there is a marginal difference in the binding energies, which shows the very slight influence of Ag decoration on the $CdMoO_4$ surface, with an upshift in binding energies of ~0.3. This shows that the coordination environment surrounding Ag was not influenced by $CdMoO_4$.

3.6 Photocatalytic study: photocatalytic activity measurements

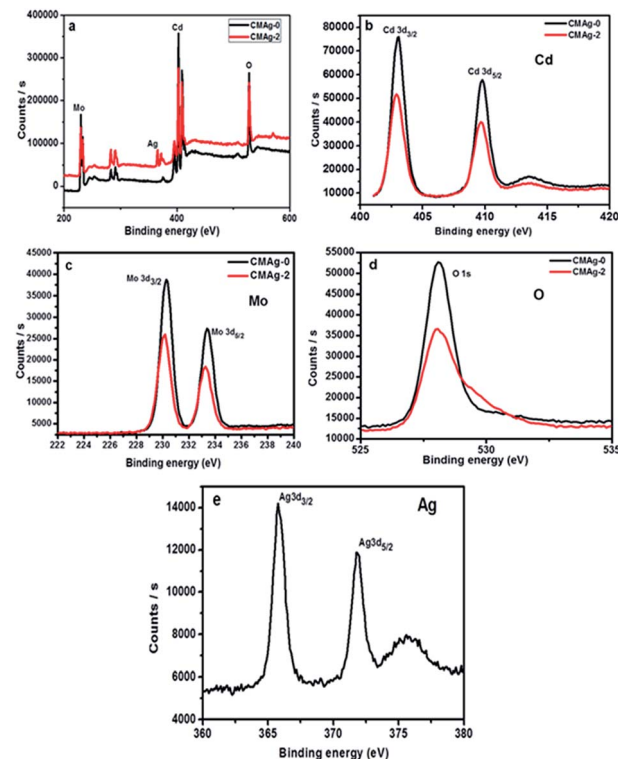As discussed earlier, Ag decorated $CdMoO_4$ is a semiconductor with a narrow band gap that lies in the visible region at room temperature. Considering the good response towards visible light, the photocatalytic activities of Ag decorated $CdMoO_4$ were investigated. Here, we report photocatalytic H_2 evolution from water under natural solar light irradiation.
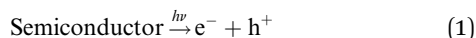
3.6.1 Photocatalytic H_2 evolution from H_2O splitting. The photocatalytic activity of hydrogen generation of $CdMoO_4$ and Ag decorated $CdMoO_4$ were studied under solar light irradiation using methanol as a scavenger electron donor. A series of experiments were performed using different concentrations of Ag nanoparticles on the surface of $CdMoO_4$ and the results are given in Table 1. The experimental results showed that the maximum hydrogen generation, *i.e.* 2465 µmol h^{-1} g^{-1}, is obtained for sample CMAg-2, whereas pure $CdMoO_4$ (CMAg-0), 0.5% Ag decorated $CdMoO_4$ (CMAg-0.5), 1% Ag decorated $CdMoO_4$ (CMAg-1) and 3% Ag decorated $CdMoO_4$ (CMAg-3) give 177, 455, 1078, and 2194 µmol h^{-1} g^{-1}, respectively. Fig. 11 shows time-dependent hydrogen generation using as-synthesized $CdMoO_4$ and Ag decorated $CdMoO_4$ nanostructures. The linearity of the graph shows the continuous and stable hydrogen rate for hydrogen generation. However, pure $CdMoO_4$ shows poor hydrogen evolution due to its wide band gap (3.2 eV).[49] In the present case, the maximum hydrogen production, *i.e.* 2465 µmol h^{-1} g^{-1}, was obtained for sample 2% Ag decorated $CdMoO_4$ (CMAg-2), which reveals that most charge carrier electrons are available for proton reduction. In the past, Guzman *et al.*[50] reported that methanol suppresses the oxygen evolution rate through the formation of free radicals and also reacts with VB holes irreversibly to reduce the charge carrier
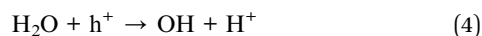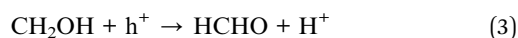
Table 1 The H_2 generation rates for as-synthesized $CdMoO_4$ and Ag–$CdMoO_4$

Sr. no.	Sample	H_2 evolution rate ($\mu mol\ h^{-1}\ g^{-1}$)
1	CMAg-0	177
2	CMAg-0.5	455
3	CMAg-1	1078
4	CMAg-2	2465
5	CMAg-3	2194

recombination rate, which affects quantum efficiency. The mechanism of photocatalytic hydrogen generation from water has been well reported. In this, the semiconductor photocatalyst after interaction with solar light with an energy greater than or equal to the band gap energy generates electrons (in the CB) and holes (in the VB). It causes redox reactions of adsorbed species on a semiconducting material. The photogenerated holes from VB oxidize methanol and get adsorbed on the surface of the semiconductor, producing protons (H^+) and free radicals, while the electrons from CB reduce H^+ ions into molecular hydrogen.[51]

$$Semiconductor \xrightarrow{h\nu} e^- + h^+ \qquad (1)$$

Oxidation:

$$CH_3OH + h^+ \rightarrow CH_2OH + H^+ \qquad (2)$$

$$CH_2OH + h^+ \rightarrow HCHO + H^+ \qquad (3)$$

$$H_2O + h^+ \rightarrow OH + H^+ \qquad (4)$$

Reduction:

$$H^+ + 2e^- \rightarrow H_2 \qquad (5)$$

It is exciting to discuss the improved photocatalytic activity in the present case. It has been well reported that the photocatalytic activity of a photocatalyst depends on its hierarchical morphology, specific surface area, visible light absorption capability, the diffusion rate of charge carriers, electronic structure and, more specifically, on the charge carrier separation rate. The effective separation of electron–hole pairs is attributed to enhanced optical absorption, which is caused by the SPR effect of Ag NPs and high conductivity due to the interaction between metallic Ag and $CdMoO_4$. Previous reports show that decoration of Ag clusters on the surface of the semiconductor tunes the surface properties and improves the interfacial charge separation efficiency between the noble metal and the semiconductor photocatalyst.[52,53] Furthermore, the band structure of the semiconductor also affects the photocatalytic activity. In the case of $CdMoO_4$, the VB is predominantly contributed by occupied O 2p orbitals and Cd 4S orbitals, whereas the bottom of the conduction band consists of empty Mo 4d orbitals. Thus, the HOMO (highest occupied molecular orbital) consists of O 2p and the LUMO (lowest unoccupied molecular orbital) consists of Mo 4d. $CdMoO_4$ absorbs light in the UV region (3.2 eV) due to charge transfer between Mo and O atoms from MoO_4^{2-}.[54,55]

On the other hand, after the decoration of Ag nanoparticles on the surface of $CdMoO_4$ the band gap energy is enhanced towards a higher wavelength, which might accelerate the photoreduction reaction under sunlight. The enhanced photocatalytic activity being ascribed to the charge carrier recombination rate being effectively suppressed by the decoration of Ag on $CdMoO_4$ is supported by the PL study. However, it is expected that there will be defect states within the $CdMoO_4$ semiconductor. These defects states have low density limiting the visible light absorption. However, Ag decoration on $CdMoO_4$ offers a platform for combining together semiconducting properties with the SPR synergistic behavior of the noble metal to improve overall photocatalytic performance, which could
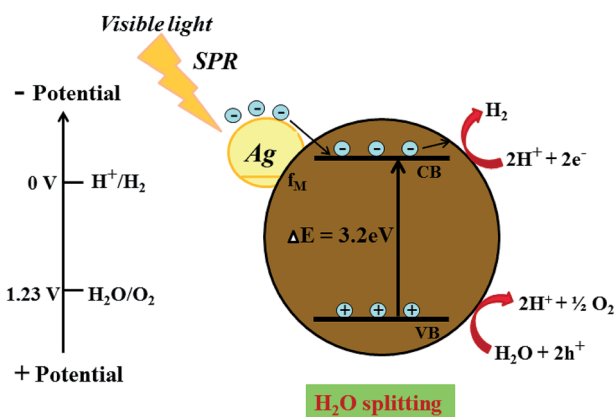
Fig. 10 Schematic representation for the proposed photocatalysis mechanism of H_2 generation on an Ag @cdMoO$_4$ nanocomposite photocatalyst under natural solar light.
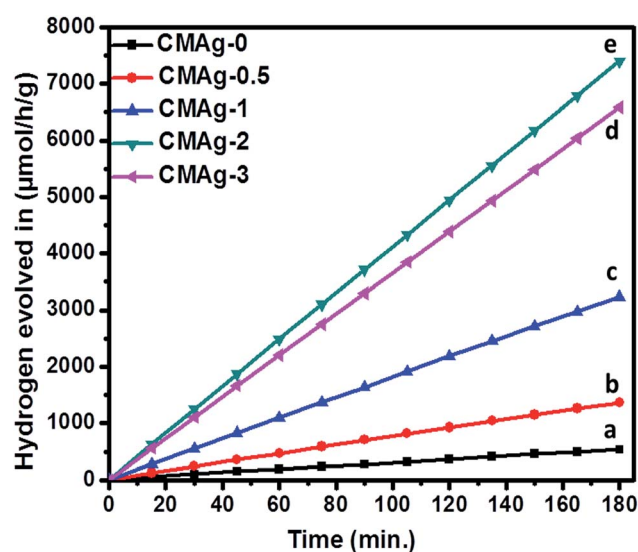
Fig. 11 Photocatalytic hydrogen generation *via* H_2O splitting with (a) CMAg-0 (black) (b) CMAg-0.5 (red) (c) CMAg-1 (blue), (d) CMAg-2 (green), (e) CMAg-3 (pink).

lead to an enhanced electric field in the visible region, which would enhance photoactivity.[56,57] Ag was used to produce a Schottky barrier to facilitate electron capture by providing chemically active sites where relevant chemical transformations can take place with lower activation energy barriers than in the semiconductor material. A photocatalysis mechanism for H_2 generation under natural solar light is proposed in Fig. 10. This indicates that the recombination rate of the CB electrons with the VB holes was retarded significantly by Ag inlay and the electron lifetime was extended. In this type of system, both charge carriers (electrons and holes) diffuse to the surface of the semiconductor where they drive the two half reactions at the specifically designed sites. The presence of Ag(0) favours absorption in the visible region and proceeds with the migration of photo-induced electrons to the CB of $CdMoO_4$.[58] Therefore, energetic charge carrier electrons reach the surface of the semiconductor to be involved in the reduction process to produce H_2.[59] 2% Ag shows good photocatalytic activity while 3% Ag shows lower photocatalytic activity due to the high concentration of Ag, which may act as a recombination center. Furthermore, a reusability study clearly shows the stable evolution of hydrogen. (ESI-S1 and Table S2†).

4. Conclusions

In summary, we have demonstrated a facile hydrothermal route for the synthesis of $CdMoO_4$ with *in situ* decoration by Ag nanoparticles. A morphological study shows that 5 nm sized spherical Ag nanoparticles are decorated on a $CdMoO_4$ nanoprism. The photocatalytic hydrogen generation activity of the as-synthesized $Ag@CdMoO_4$ photocatalyst was found to be higher than that of pristine $CdMoO_4$. Among all the photocatalysts, 2% Ag decorated $CdMoO_4$ shows enhanced hydrogen generation: *i.e.* 2465 μmol h^{-1} g^{-1} under natural sunlight. Moreover, it was found that, as the concentration of Ag nanoparticles increases, the photocatalytic hydrogen generation rate increases. Thus, the presence of Ag nanoparticles on $CdMoO_4$ promotes the effective separation of photogenerated electron–hole pairs and also shows surface plasma resonance excitation, which enhances the hydrogen generation rate.

Conflicts of interest

No conflict of interest.

Acknowledgements

References

1 J. A. Turner, *Science*, 1999, **285**, 687–689.

2 M. Faraji, M. Yousefi, S. Yousefzadeh, M. Zirak, N. Naseri, T. H. Jeon, W. Choi and A. Z. MoshfeghIt, *Energy Environ. Sci.*, 2019, **12**, 59–95.

3 A. Fujishima and K. Honda, *Nature*, 1972, **238**, 37–38.

4 R. Liu, Z. Zheng, J. Spurgeon and X. Yang, *Energy Environ. Sci.*, 2014, **7**, 2504–2517.

5 X. Zou, X. Huang, A. Goswami, R. Silva, B. R. Sathe, E. Mikmeková and T. Asefa, *Angew. Chem., Int. Ed.*, 2014, **53**, 4372–4376.

6 S. Sharma and S. K. Ghoshal, *Renewable Sustainable Energy Rev.*, 2015, **43**, 1151–1158.

7 T. R. Cook, D. K. Dogutan, S. Y. Reece, Y. Surendranath, T. S. Teets and D. G. Nocera, *Chem. Rev.*, 2010, **110**, 6474–6502.

8 A. K. Kulkarni, C. S. Praveen, Y. A. Sethi, R. P. Panmand, S. S. Arbuj, S. D. Naik, A. V. Ghule and B. B. Kale, *Dalton Trans.*, 2017, **46**, 14859–14868.

9 V. S. Haussener, C. Xiang, J. M. Spurgeon, S. Ardo, N. S. Lewis and A. Z. Weber, *Energy Environ. Sci.*, 2012, **5**, 9922–9935.

10 H. G. Park and J. K. Holt, *Energy Environ. Sci.*, 2010, **3**, 1028–1036.

11 B. Archana, K. Manjunath, G. Nagaraju, K. B. Chandra Sekhar and N. Kottam, *Int. J. Hydrogen Energy*, 2017, **42**, 5125–5131.

12 P. A. Bharad, A. V. Nikam, F. Thomas and C. S. Gopinath, *ChemistrySelect*, 2018, **3**, 12022–12030.

13 S. P. Adhikari, Z. D. Hood, K. L. More, I. Ivanov, L. Zhang, M. Gross and A. Lachgar, *RSC Adv.*, 2015, **5**, 54998–55005.

14 Y. A. Sethi, R. P. Panmand, S. R. Kadam, A. K. Kulkarni, S. K. Apte, S. D. Naik, N. Munirathnam, M. V. Kulkarni and B. B. Kale, *J. Colloid Interface Sci.*, 2017, **487**, 504–512.

15 J. Zhang, Y. Wang, J. Zhang, Z. Lin, F. Huang and J. Yu, *ACS Appl. Mater. Interfaces*, 2013, **5**, 1031–1037.

16 M. Li, X. He, Y. Zeng, M. Chen, Z. Zhang, H. Yang, P. Fang, X. Lu and Y. Tong, *Chem. Sci.*, 2015, **6**, 6799–6805.

17 S. Sfaelou, L. C-Pop, O. Monfort, V. Dracopoulos and P. Lianos, *Int. J. Hydrogen Energy*, 2016, **41**, 5902–5907.

18 F. E. Osterloh, *Chem. Mater.*, 2008, **20**, 35–54.

19 X. Chen, S. Shen, L. Guo and S. S. Mao, *Chem. Rev.*, 2010, **110**(11), 6503–6570.

20 M. Sathish, B. Viswanathan, R. P. Viswanath and C. S. Gopinath, *Chem. Mater.*, 2005, **17**, 6349–6353.

21 A. Bhirud, S. Sathaye, R. Waichal, C.-J. Park and B. Kale, *J. Mater. Chem. A*, 2015, **3**, 17050–17063.

22 Q. Xiang, J. Yu and M. Jaroniec, *J. Am. Chem. Soc.*, 2012, **134**, 6575–6578.

23 W. Zhao, W. Ma, C. Chen, J. Zhao and Z. Shuai, *J. Am. Chem. Soc.*, 2004, **126**, 4782–4783.

24 Y. Shi, Y. Wang, J. I. Wong, A. Y. S. Tan, C.-L. Hsu, L.-J. Li, Y.-C. Lu and H. Y. Yang, *Sci. Rep.*, 2013, **3**, 2169–2177.

25 M.-L. Tsai, S.-H. Su, J.-K. Chang, D.-S. Tsai, C.-H. Chen, C.-I. Wu, L.-J. Li, L.-J. Chen and J.-H. He, *ACS Nano*, 2014, **8**, 8317–8322.

26 Q. Dai, G. Zhang, P. Liu, J. Wang and J. Tang, *Inorg. Chem.*, 2012, **51**, 9232–9239.

27 L. Zhou, W. Wang, H. Xu and S. Sun, *Cryst. Growth Des.*, 2008, **8**, 3595–3601.

28 (a) Y. Liu, L. Ren, X. Qi, Y. Wang, X. Liu and J. Zhong, *RSC Adv.*, 2014, **4**, 8772–8776; (b) S. R. Kadam, R. P. Panmand, S. P Tekale, S. K. Khore, C. Terashima, S. W. Gosavi, A. Fujishima Bharat and B. Kale, *RSC Adv.*, 2018, **8**(25), 13764–13771.

29 (a) P. A. Bharad, K. Sivaranjania and C. S. Gopinath, *Nanoscale*, 2015, **7**, 11206–11215; (b) P. Wang, B. Huang, Y. Dai and M.-H. Whangbo, *Phys. Chem. Chem. Phys.*, 2012, **14**, 9813–9825; (c) X. Zhang, Y. L. Chen, R.-S. Liu and D. P. Tsai, *Rep. Prog. Phys.*, 2013, **76**, 046401.

30 J. Xiong, Z. Li, J. Chen, S. Zhang, L. Wang and S. Dou, *ACS Appl. Mater. Interfaces*, 2014, **6**, 15716–15725.

31 R. Adhikari, S. Malla, G. Gyawali, T. Sekino and S. W. Lee, *Mater. Res. Bull.*, 2013, **48**, 3367–3373.

32 S. R. Shieh, L. C. Ming and A. Jayaraman, *J. Phys. Chem. Solids*, 1996, **57**, 205–209.

33 Y. Liu, L. Ren, X. Qi, Y. Wang, X. Liu and J. Zhong, *RSC Adv.*, 2014, **4**, 8772–8778.

34 S. M. H-Mashkani, M. Maddahfar and A. S-Nasab, *J. Mater. Sci.: Mater. Electron.*, 2016, **27**, 467–474.

35 P. V. Pimpliskar, S. C. Motekar, G. G. Umarji, W. Lee and S. S. Arbuj, *Photochem. Photobiol. Sci.*, 2019, **18**, 1503–1511.

36 R. Grasser, E. Pitt, A. Scharmann and G. Zimmerer, *Phys. Status Solidi B*, 1975, **69**, 359–368.

37 Y. Li, S. Tan, J. Jiang, Z. Huang and X. Tan, *CrystEngComm*, 2011, **13**, 2649–2655.

38 F. X. Redl, K.-S. Cho, C. B. Murray and S. O'Brien, *Nature*, 2003, **423**, 968–971.

39 S. Link and M. A. El-Sayed, *J. Phys. Chem. B*, 1999, **103**, 8410–8426.

40 S. S. Patil, M. G. Mali, M. S. Tamboli, D. R. Patil, M. V. Kulkarni, H. Yoon, H. Kim, S. S. Al-Deyab, S. S. Yoon, S. S. Kolekar and B. B. Kale, *Catal. Today*, 2016, **260**, 126–134.

41 Z. Zhao, Z. Sui, X. Wei, J. Zuo, X. Zhang, R. Dai, Z. Zhang and Z. Dinga, *CrystEngComm*, 2015, **17**, 7905–7914.

42 P. Godlewska, E. Tomaszewicz, L. Macalik, J. Hanuza, M. Ptak, P. E. Tomaszewski, M. Mączka and P. Ropuszyńska-Robak, *Mater. Chem. Phys.*, 2013, **139**, 890–896.

43 P. Godlewska, E. Tomaszewicz, L. Macalik, J. Hanuza, M. Ptak, P. E. Tomaszewski and P. Ropuszyńska-Robak, *J. Mol. Struct.*, 2013, **1037**, 332–337.

44 L. Yang, X. Jiang, W. Ruan, J. Yang, B. Zhao, W. Xu and J. R. Lombardi, *J. Phys. Chem. C*, 2009, **113**, 16226–16231.

45 J. Bi, Z. Zhou, M. Chen, S. Liang, Y. He, Z. Zhang and L. Wu, *Appl. Surf. Sci.*, 2015, **349**, 292–298.

46 A. K. Kulkarni, R. P. Panmand, Y. A. Sethi, S. R. Kadam, D. R. Patil, A. V. Ghule and B. B. Kale, *New J. Chem.*, 2018, **42**, 17597–17605.

47 H. Zhang, C.-G. Niu, X.-J. Wen, Y. Wang and G.-M. Zeng, *Catal. Commun.*, 2016, **86**, 124–128.

48 P. Thakur, S. S. Joshi and K. R. Patil, *Appl. Surf. Sci.*, 2010, **257**, 1390–1394.

49 L. R. Lou, L. Lian, L. H. Zhang and J. Y. Li, *Mater. Lett.*, 2013, **109**, 306–308.

50 F. Guzman, S. S. C. Chuang and C. Yang, *Ind. Eng. Chem. Res.*, 2013, **52**, 61–65.

51 A. K. Kulkarni, R. P. Panmand, Y. A. Sethi, S. R. Kadam, S. P. Tekale, G.-H. Baeg, A. V. Ghule and B. B. Kale, *Int. J. Hydrogen Energy*, 2018, **43**, 19873–19884.

52 Y. Chen, Y. Wang, W. Li, Q. Yang, Q. Hou, L. Wei, L. Liu, F. Huang and M. Ju, *Appl. Catal., B*, 2017, **210**, 352–367.

53 S. Zhao, Z. Cheng, L. Khang, M. Li and Z. Gao, *RSC Adv.*, 2017, **7**, 50064–50071.

54 L. Zhen, W. S. Wang, C. Y. Xu, W. Z. Shao, M. M. Ye and Z. L. Chen, *Scr. Mater.*, 2008, **58**, 461–464.

55 M. Fujita, M. Itoh, T. Katagiri, D. Iri, M. Kitaura and V. B. Mikhailik, *Phys. Rev. B: Condens. Matter Mater. Phys.*, 2008, **77**, 155118.

56 Y.-C. Pu, G. Wang, K.-D. Chang, Y. Ling, Y.-K. Lin, B. C. Fitzmorris, C.-M. Liu, X. Lu, Y. Tong, J. Z. Zhang, Y.-J. Hsu and Y. Li, *Nano Lett.*, 2013, **13**, 3817–3823.

57 Z. W. Seh, S. Liu, M. Low, S. Y. Zhang, Z. Liu, A. Mlayah and M. Y. Han, *Adv. Mater.*, 2012, **24**, 2310–2314.

58 S. K. Khore, S. R. Kadam, S. D. Naik, B. B. Kale and R. S. Sonawane, *New J. Chem.*, 2018, **42**, 10958–10968.

59 S. S. Rayalu, D. Jose, M. M. Joshi, P. A. Mangrulkar, K. Shrestha and K. Klablunde, *Appl. Catal., B*, 2010, **257**, 1390–1394.